

## Ultra-high resolution brain metabolite mapping at 7 T by short-TR Hadamard-encoded FID-MRSI<sup>☆</sup>

Gilbert Hangel<sup>a</sup>, Bernhard Strasser<sup>a</sup>, Michal Považan<sup>b</sup>, Eva Heckova<sup>a</sup>, Lukas Hingerl<sup>a</sup>, Roland Boubela<sup>a</sup>, Stephan Gruber<sup>a</sup>, Siegfried Trattnig<sup>b</sup>, Wolfgang Bogner<sup>a,\*</sup>

<sup>a</sup> High Field MR Center, Department of Biomedical Imaging and Image-guided Therapy, Medical University of Vienna, Austria

<sup>b</sup> High Field MR Center, Department of Biomedical Imaging and Image-guided Therapy, Medical University of Vienna, Christian Doppler Laboratory for Clinical Molecular MR Imaging, Austria

### ARTICLE INFO

#### Keywords:

Proton magnetic resonance spectroscopic imaging  
7 T  
Ultra-high resolution spectroscopic imaging  
Parallel imaging  
Brain  
Hadamard encoding

### ABSTRACT

MRSI in the brain at  $\geq 7$  T is a technique of great promise, but has been limited mainly by low  $B_0/B_1^+$ -homogeneity, specific absorption rate restrictions, long measurement times, and low spatial resolution. To overcome these limitations, we propose an ultra-high resolution (UHR) MRSI sequence that provides a  $128 \times 128$  matrix with a nominal voxel volume of  $1.7 \times 1.7 \times 8$  mm<sup>3</sup> in a comparatively short measurement time. A clinically feasible scan time of 10–20 min is reached via a short TR of 200 ms due to an optimised free induction decay-based acquisition with shortened water suppression as well as parallel imaging (PI) using Controlled Aliasing In Parallel Imaging Results IN Higher Acceleration (CAIPIRINHA). This approach is not limited to a rectangular region of interest in the centre of the brain, but also covers cortical brain regions. Transversal pulse-cascaded Hadamard encoding was able to further extend the coverage to 3D-UHR-MRSI of four slices ( $100 \times 100 \times 4$  matrix size), with a measurement time of 17 min. Lipid contamination was removed during post-processing using L2-regularisation. Simulations, phantom and volunteer measurements were performed. The obtained single-slice and 3D-metabolite maps show the brain in unprecedented detail (e.g., hemispheres, ventricles, gyri, and the contrast between grey and white matter). This facilitates the use of UHR-MRSI for clinical applications, such as measurements of the small structures and metabolic pathologic deviations found in small Multiple Sclerosis lesions.

### 1. Introduction

Proton magnetic resonance spectroscopic imaging (MRSI) in the brain is a powerful non-invasive metabolic imaging modality that enables an investigation of the spatial distribution of multiple metabolites simultaneously. Apart from the application for basic research,

the detection of metabolic changes caused by brain tumours, epilepsy, Multiple Sclerosis (MS) or other neurodegenerative diseases can assist in clinical research and diagnosis (Hetherington et al., 2014; Pan et al., 2013; Ratai et al., 2008; Srinivasan et al., 2010). Particularly for the investigation of the spatially heterogeneous composition of glioma in particular in the infiltrative form and MS lesions that typically have

**Abbreviations:** Ac, acetate; AD, acquisition delay; CAIPIRINHA, controlled aliasing in parallel imaging results in higher acceleration; Cho, choline; CRLB, Cramér-Rao lower bound; Cr, creatine; CSF, cerebrospinal fluid; DIR, double inversion recovery; EPSI, echo-planar spectroscopic imaging; FA, flip angle; FID, free induction decay; FIDLOVS, slice-selective FID acquisition, localized by outer volume suppression; FOV, field of view; FWHM, full width at half maximum; Gln, glutamine; Glu, glutamate; Glx, glutamate + glutamine; GM, grey matter; GRAPPA, generalized autocalibrating partially parallel acquisition; GRE, gradient echo; HSI, Hadamard spectroscopic imaging; Ins, inositol; LSF, lipid suppression factor; MP2RAGE, magnetization-prepared 2 rapid acquisition gradient echoes; MS, multiple sclerosis; MUSICAL, multichannel spectroscopic data combined by matching image calibration data; NAA, N-acetyl-aspartate; NAAG, N-acetyl-aspartyl glutamate; PCr, phosphocreatine; PI, parallel imaging; PRESS, point-resolved spectroscopy; PSF, point-spread function; R, parallel imaging acceleration factor; ROI, region of interest; SAR, specific absorption rate; semi-LASER, semi-localized adiabatic selective refocusing; SENSE, sensitivity encoding; SNR, signal-to-noise ratio; SSL, single-slice; SWAMP, sequence for water suppression with adiabatic modulated pulses; tCho, choline-containing compounds; tCr, Cr + PCr; tNAA, NAA + NAAG; UHR, ultra-high resolution; WET, water suppression enhanced through T<sub>1</sub> effects; WM, white matter; WS, water suppression

<sup>☆</sup> Category: *Methods and Modeling*. Parts of the measurements presented in this manuscript were presented at: 1) Phantom measurements: *3D Metabolic Mapping of the Brain at 7 T by Pulse-Cascaded Hadamard Encoding with Short Acquisition Delay* - Hangel et al., International Society for Magnetic Resonance in Medicine, 21st Annual Meeting, presentation number 2022, 2013, Salt Lake City, Utah, United States of America and 2) Single slice UHR-MRSI measurements: *Metabolic mapping in the brain using ultra-high resolution MRSI at 7 T* - Hangel et al., International Society for Magnetic Resonance in Medicine, 24th Annual Meeting, presentation number 0387, 2016, Singapore.

\* Correspondence to: High Field MR Center, Department of Biomedical Imaging and Image-guided Therapy, Medical University of Vienna, Lazarettgasse 14, 1090 Wien, Vienna, Austria.

E-mail address: [wolfgang.bogner@meduniwien.ac.at](mailto:wolfgang.bogner@meduniwien.ac.at) (W. Bogner).

<http://dx.doi.org/10.1016/j.neuroimage.2016.10.043>

Accepted 26 October 2016

Available online xxxx

1053-8119/© 2016 The Author(s). Published by Elsevier Inc. This is an open access article under the CC BY-NC-ND license (<http://creativecommons.org/licenses/by/4.0/>).

dimensions in the range of only 3–6 mm, the resolution of previous MRS and MRSI methods was insufficient. Thus, increasing the resolution of MRSI is an important step toward increasing the clinical utility. Ultra-high field MR systems (i.e.,  $\geq 7$  T) offer significant advantages for MRSI that can be used to that end, but before these can be fully exploited several limitations must be addressed.

### 1.1. Advantages and limitations of MRSI at $\geq 7$ T

MRSI benefits from higher  $B_0$  due to an increased signal-to-noise ratio (SNR) that can be translated into higher spatial resolutions or faster measurements. The increased spectral dispersion facilitates the separation and quantification of neighbouring resonances (Moser et al., 2012).

At  $\geq 7$  T, MRSI suffers from more pronounced constraints compared to lower  $B_0$  (Moser et al., 2012) including specific absorption rate (SAR) restrictions, shorter  $T_2$ s that penalise the use of long echo times (TEs), lower  $B_0/B_1^+$ -homogeneity that decreases spectral quality and complicates water/lipid-suppression, and larger chemical shift displacement errors (CSDEs). In addition, the general limitations of conventional MRSI sequences apply: point-spread functions (PSF) for low matrix sizes lead to poor slice profiles, subject movement and long measurement times.

### 1.2. 7 T MRSI – state of the art

Previous research has addressed these constraints. The signal loss to  $T_2$ -relaxation and J-evolution can be overcome by shortening the TE (Ardievich et al., 2009; Boer et al., 2011) or by direct free induction decay (FID)-acquisition (Bogner et al., 2012; Henning et al., 2009). Localisation by semi-localized adiabatic selective refocusing (semi-LASER) (Scheenen et al., 2008) or point-resolved spectroscopy (PRESS) (Balchandani et al., 2008; Xu et al., 2008) were successfully adapted to 7 T, but are limited to a region of interest (ROI) in the centre of the brain.

Non-Cartesian trajectories such as spiral MRSI (Andronesi et al., 2012) or echo-planar spectroscopic imaging (EPSI) (Lecocq et al., 2014) accelerate measurements considerably at lower field strengths ( $\leq 3$  T), but the increased spectral bandwidth requirements at  $\geq 7$  T has limited the achievable resolutions. Thus far, EPSI was only applied to systems with specialised, stronger head gradient systems (Otazo et al., 2006). Parallel imaging (PI) is another option for measurement acceleration, which benefits from  $\geq 7$  T (Wiesinger et al., 2004). Sensitivity-encoding (SENSE) (Kirchner et al., 2015; Zhu et al., 2013) as well as generalized autocalibrating partially parallel acquisitions (GRAPPA) (Hangel et al., 2015), have thus far been demonstrated for 7 T.

Lipid suppression for 7 T was adapted in the context of higher SAR demands and field inhomogeneities. While high in-plane resolutions and Hamming filtering can reduce lipid contamination via improvement of the PSF (Bogner et al., 2012), several sequence-based lipid suppression schemes were proposed, such as FIDLOVS (FID acquisition, Localized by Outer Volume Suppression) (Henning et al., 2009), SWAMP (Sequence for Water suppression [WS] with Adiabatic Modulated Pulses) extended to simultaneous lipid/water suppression (Boer et al., 2011), spatial-spectral adiabatic inversion pulses (Balchandani and Spielman, 2008), simultaneous water/lipid suppression using adiabatic full-passage pulses (Zhu et al., 2013) or non-selective double inversion recovery-based lipid suppression (Hangel et al., 2015). These methods typically require long TRs, are limited to a restricted ROI inside the brain or reduce SNR. Additional hardware (Boer et al., 2015; Hetherington et al., 2010) allows further improved lipid suppression with fewer limitations for the sequence itself, but is not widely available. Higher-order shims (Hetherington et al., 2014; Pan et al., 2012) or parallel transmit systems (Boer et al., 2012; Emir et al., 2012) greatly improve  $B_0$ - and  $B_1^+$ -homogeneity. These sub-

stantially support (frequency-selective) suppression techniques.

Multi-slice MRSI is often desirable to cover the entire brain region of interest. To avoid an excessive increase in measurement time, and reduction in  $B_0$ -homogeneity over large volumes at  $\geq 7$  T, the covered ROI is often kept as small as possible. However, the sampling of only few slices (e.g. 2–8) via phase encoding provides only poor localisation due to the PSF. Alternatively, interleaved slice-selective multi-slice MRSI (Boer et al., 2012) was proposed for 7 T. Another approach is slice encoding via a pulse-cascaded Hadamard scheme (Goelman et al., 2007). This provides higher SNR than interleaved single-slice acquisitions and offers better slice profiles than phase encoding.

### 1.3. Purpose

We propose a high-resolution FID-acquisition sequence for ultra-high resolution (UHR)-MRSI at 7 T. Combined TR reduction and PI shorten measurement times to an extent that makes UHR-MRSI clinically feasible. Pulse-cascaded Hadamard encoding allows the expansion to 3D-UHR-MRSI. This allows the visualisation of biochemical changes in the brain in unprecedented detail, e.g. in order to resolve small Multiple Sclerosis lesions.

## 2. Materials and methods

### 2.1. Subjects and hardware

Seven healthy volunteers (five males, two females; median age, 28 years; range, 26–34 years) participated in this study. Institutional Review Board approval and written, informed consent were obtained. We performed measurements on a 7 T whole-body MR scanner (Magnetom, Siemens Healthcare, Erlangen, Germany) with a 7T\_SC72CD gradient system with 70 mT/m total gradient strength and 200 mT/m/s nominal slew rate. A head coil with a 32-channel receive coil array combined with a volume coil for transmission (Nova Medical, Wilmington, MA, USA) was used.

### 2.2. Sequence design

Our main design goal was the acceleration of MRSI scans to realise single-slice and 3D UHR metabolic mapping in clinically feasible scan times. This was accomplished by a) reducing the minimum TR via shortened water suppression and signal readout, b) efficient parallel imaging (Strasser et al., 2016) and c) pulse-cascaded Hadamard encoding (Goelman et al., 2007) for 3D coverage.

The resulting FID-MRSI sequence was similar to earlier approaches (Bogner et al., 2012; Strasser et al., 2013), but allowed a shorter TR of 200 ms, matrix sizes up to  $128 \times 128$  and up to four Hadamard-encoded slices. The ultra-short AD of 1.3–4.3 ms (depending on the slice) led to a high SNR due to negligible  $T_2$ -decay and J-modulation. As the short TR did not allow for extensive lipid-suppression schemes, lipid contamination was removed using L2-regularisation (Bilgic et al., 2013) during post-processing.

#### 2.2.1. TR reduction

Originally, the WET (Water suppression Enhanced through  $T_1$  effects) scheme (Ogg et al., 1994) was designed for 1.5 T as insensitive to variations in  $B_1^+$  and  $T_1$  relaxation. This WET scheme had to be adapted for our 7 T system. The WET module is typically implemented using three sub-modules (each consisting of a 9 ms Gauss suppression RF pulse with a bandwidth of 100 Hz and a 51 ms spoiler gradient for a total duration  $\tau$  of 60 ms). This results in a total WS duration of 180 ms. The increased gradient performance of our scanner allowed a substantially reduced  $\tau$  (i.e., tested for values ranging from 10 to 60 ms). In addition, we implemented a 4th suppression pulse as proposed by (Ogg et al., 1994) to increase the suppression stability (defined by the residual water magnetisation for a variation of  $B_1^+$  of  $\pm$

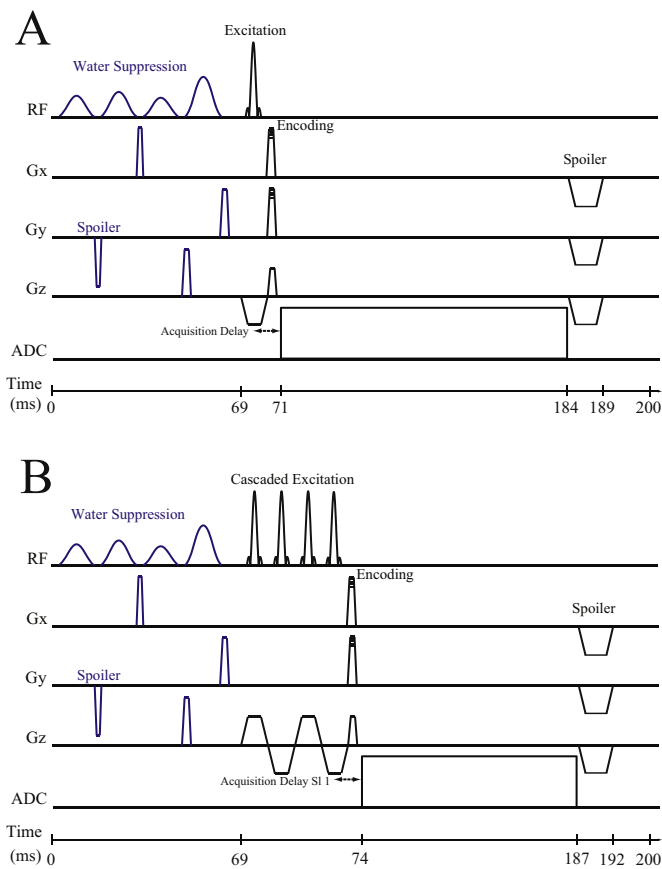


**Fig. 1.** UHR-FID-MRSI scheme (not to scale) for A) a single slice, and B) Hadamard-encoded multi-slice utilising cascaded excitation, with one excitation pulse per slice. Optimised use of the gradient system, together with a shorter readout window and the FID approach allow TRs in the range of 200 ms. The acquisition delay is defined from the centre of the excitation pulse to the readout start.

15%) to compensate for the increased  $B_1^+$ -inhomogeneities at 7 T.

As a second step, we reduced the readout duration by decreasing the number of sampling points (including overampling) from 2048 to 1024 and using a shorter dwell time of 111  $\mu$ s (i.e., 9000 Hz readout bandwidth), resulting in a readout duration of 113 ms compared to the prior 343 ms.

Thereby, TRs in the range of 200 ms could be realised, as depicted by the sequence scheme in Fig. 1A.

### 2.2.2. Parallel Imaging - CAIPIRINHA

The application of CAIPIRINHA (Controlled Aliasing In Parallel Imaging Results IN Higher Acceleration) (Strasser et al., 2016) allowed a further reduction of measurement times. In contrast to traditional GRAPPA-based parallel imaging, which leaves out entire lines in k-space, CAIPIRINHA leaves out more complicated k-space pattern to improve the reconstruction efficiency. In both cases the missing k-space points are then reconstructed using information from the array coil and additionally acquired autocalibration signal lines. Our implementation of CAIPIRINHA acquires autocalibration signal prescans via a rapid gradient echo sequence, in  $\sim$ one second with low g-factors for accelerations  $\leq 9$  (Hangel et al., 2015).

### 2.2.3. Ultra-high resolution

By decreasing TR from  $\sim$ 600–1500 ms to 200 ms and accelerating by  $\sim 9$  via CAIPIRINHA, a total acquisition acceleration of  $\sim 30$ –70-fold can be achieved. This allowed MRSI matrix sizes of  $128 \times 128$  (i.e., nominal in-plane resolution of  $1.7 \times 1.7$  mm<sup>2</sup> and a nominal voxel volume of 23  $\mu$ l) to be realized in clinically feasible measurement times.

### 2.2.4. Hadamard spectroscopic imaging

Multi-slice MRSI was implemented via transverse pulse-cascaded Hadamard encoding to overcome limitations of conventional Hadamard spectroscopic imaging (HSI) with superimposed selection pulses at  $\geq 7$  T (Goelman et al., 2007). This approach reduced SAR requirements and CSDEs by playing out the selective RF pulses in the HSI encoded direction in rapid succession. The modification of the MRSI sequence for HSI is displayed in Fig. 1B. In general, transverse HSI allows the measurement of  $2^n$  slices ( $n=1,2,3 \dots$ ) by simultaneously selecting all these slices and repeating each excitation  $2^n$ -times with different excitation phase settings. The individual slices can be later separated with a special subtraction/addition scheme that is determined by the Hadamard matrix.

### 2.3. Simulations and parameter optimisation

We simulated the steady-state magnetisation for N-acetyl-aspartate (NAA), creatine (Cr), choline (Cho), glutamate (Glu) and myo-inositol (Ins), for the TRs of 200 ms, 600 ms, and 1500 ms to estimate the change in the signal ratios between metabolites (i.e., Cr/NAA, Cho/NAA, Glu/NAA, Ins/NAA) for different TRs. The calculations were based on reported  $T_1$  values (Xin et al., 2013). The optimal average flip angle (FA)/Ernst angle for the main metabolites was calculated as geometric average (Bottomley and Ouwkerk, 1994). The relative SNR and sensitivity calculations were based on studies by (Pohmann et al., 1997).

### 2.4. Measurement protocols

The *in vivo* MRSI protocols included additional MRI scans: MP2RAGE (magnetization-prepared 2 rapid acquisition gradient echoes) (Marques et al., 2010) with a 4:39 min scan time, and a pre-saturation turbo-FLASH-based  $B_1^+$ -mapping sequence (Chung et al., 2010; Klose, 1992) to optimise the effective MRSI excitation FA. Second-order field map-based  $B_0$ -shimming was used. CAIPIRINHA calibration data and receiver noise-prescans were integrated into the MRSI sequences and were utilised for PI reconstruction (Hangel et al., 2015) and coil combination (Strasser et al., 2013). In total, imaging, shimming, and field of view (FOV) placement (typically placed transversally above the ventricles) required around 15–20 min.

All MRSI protocols shared the following settings: AD of 1.3 ms (i.e., 1.3–4.3 ms for 4-slice HSI); FOV of  $220 \times 220$  mm<sup>2</sup>; 10 mm slice thickness for single slice and 8 mm for multi-slice scans; elliptical k-space sampling with a spiral-like scheme starting at the k-space centre; three-lobe SINC excitation pulses with 0.6 ms duration and a flip angle of 29° for TR 200 ms (calculated  $B_1$ : 9.14  $\mu$ T) and 45° for TR 600 ms (calculated  $B_1$ : 14.18  $\mu$ T). WET water suppression was implemented with a four-pulse scheme and a 100 Hz pulse bandwidth, with a total duration of 64 ms. Five main protocols were used to evaluate *in vivo* MRSI protocols (Tbl. 1). Five *in vivo* MRSI protocols were defined (Tbl. 1). Further protocols for validation of water suppression and HSI performance are described in the subsections 2.4.1 and 2.4.3.

#### 2.4.1. Volunteer measurements – Water suppression

To exclude any negative effects due to shortening of the WS module, fixed MRSI sequence parameters (i.e.,  $32 \times 32$  matrix, TR 600 ms, and acceleration R of 9, 1:09 min) were used for different WS settings: no WS; three pulse-WS ( $\tau$  60 ms; total duration 180 ms); and four pulse-WS (variable  $\tau$  of 10, 11, 12, 15, 20, 30, 40, 50 and 60 ms; total duration 40–240 ms). Suppression efficiency was defined as  $\frac{SNR_{WS}}{SNR_{no WS}}$  of the water peak for each voxel, averaged over the whole slice and compared between the different WS scans. The spectral quality was compared between the different WS measurements.

**Table 1**

Overview of the MRSI measurement protocols used and their relevant differences. The protocol names defined here are used in the whole text. R is the CAIPIRINHA acceleration factor. The in-plane FOV for all protocols was 220 mm×220 mm. For the TR 200 ms protocols, an excitation flip angle of 29° and an ADC with 1024 complex sampling points/9000 Hz readout bandwidth was used. For the TR 600 ms protocols, a flip angle of 45° and 2048 points/6000 Hz was used.

Protocol	Matrix	TR [ms]	R	Duration [min]	Volunteers	Nominal resolution [mm <sup>3</sup> ]
#1 1SL_M128_TR200	128×128	200	1	42	3	1.7×1.7×10
#2 1SL_M64_TR600	64×64	600	4	7.5	2	3.4×3.4×10
#3 1SL_M64_TR200	64×64	200	4	2.5	2	3.4×3.4×10
#4 4SL_M64_TR200	64×64×4	200	6	7	5	3.4×3.4×8
#5 4SL_M100_TR200	100×100×4	200	6	17	5	2.2×2.2×8

#### 2.4.2. Volunteer measurements – Single-slice UHR

In order to test the feasibility of the proposed UHR-MRSI sequence *in vivo*, we measured three volunteers (all male; 34, 34, 27 y) with the fully sampled UHR protocol #1-“1SL\_M128\_TR200” (Table 1). The resulting datasets were reconstructed without undersampling as well as with artificial undersampling using 2D-CAIPIRINHA acceleration by a factor of 2, 3, 4, 5, 6 and 8. The quality of metabolic maps with different acceleration factors was compared.

In order to evaluate the impact of the changed TR and resolution on spectral quality, we compared results obtained with protocol #1-“1SL\_M128\_TR200” with those obtained in two volunteers with protocol #2-“1SL\_M64\_TR600” and protocol #3- “1SL\_M64\_TR200” (Tbl. 1).

#### 2.4.3. Phantom scans – HSI SNR and localisation

To investigate the slice localisation properties of our Hadamard encoding module, we conducted three phantom experiments.

- Slice profiles were measured in a cylindrical phantom filled with MACROL oil. The cascaded pulse scheme was inserted into a spin-echo sequence (TR 20 s, TE 300 ms, and 10 mm slice thickness, 90° flip angle) that excited a whole slice and read out the spatial excitation profile using a z-gradient during readout. Four-slice HSI measurements were conducted with adjacent slices, as well as gaps between the slices of 50, 100, 200, and 300% of the slice thickness. As a comparison, four adjacent individual slices with four averages were measured. The resulting pulse profiles and the signal bleed into the other slice positions were evaluated.
- Signal bleeding between slices was assessed in a cylindrical phantom with compartments. A small compartment was filled with a creatine (Cr) solution, while the adjacent compartments contained a 5% acetate (Ac) solution (relative concentration Ac:Cr ~5:1). A single-slice MRSI scan placed in the Cr compartment was compared to HSI-MRSI with adjacent slices or a 100% slice gap (32×32-matrix and 5 mm slice thickness for all three) that had one of the middle slices in the same position as the single slice. For reference, a single slice in the Ac compartment was measured. The contamination was calculated as the ratio of the Ac signal of the slice in the Cr compartment to the Ac signal in the Ac compartment reference slice.
- The third measurement determined the effective SNR gain compared to single-slice (1SL-)MRSI. HSI and 1SL-MRSI (42×42 matrix, 8:24 minutes measurement time per slice) were measured with the single slice and HSI-slice #3 placed identically in the Cr compartment. The average Cr SNR was compared.

#### 2.4.4. Volunteer measurements – HSI-UHR

To test the feasibility of multi-slice acquisition, we measured protocol #5- “4SL\_M100\_TR200” (Tbl. 1) in all five volunteers. Due to practical constraints of SNR and measurement time feasibility in clinical settings, we chose an acceleration factor of 6 with a reduced matrix size of 100×100×4 to remain below < 17 min scan time. With a slice gap of 2 mm between the slices, this resulted in an FOV of 220×220×38 mm<sup>3</sup>. Considering the SNR gain due to HSI and increased voxel size, but with the reduced amount of encoding steps, we expected

an SNR-increase of 5% compared to the previous un-accelerated protocol #1-“1SL\_M128\_TR200” under optimal conditions. This was evaluated experimentally by comparing protocol #1-“1SL\_M128\_TR200” and #5-“4SL\_M100\_TR200”. Robustness and quality were validated as before (2.4.2), with a focus on the resulting metabolite and metabolic ratio maps.

#### 2.5. Data processing

For offline MRSI data processing, we used an in-house-developed tool (Považan et al., ISMRM 2015, Nr. 1973) based on Matlab (R2013a, MathWorks, Natick, MA, USA), Bash (version 4.2.25, Free Software Foundation, Boston, MA, USA), and MINC (MINC tools, v2.0, McConnell Brain Imaging Center, Montreal, QC, Canada). MUSICAL (multichannel spectroscopic data combined by matching image calibration data) coil combination (Strasser et al., 2013), CAIPIRINHA reconstruction, and a spatial Hamming filter were applied. No apodisation filter or zero filling was used. Spectral fitting of the spectral range between 1.8 and 4.0 ppm used LCModel (Provencher, 2001) and included a measured macromolecule background in the basis-set (Považan et al., 2015). Possible lipid contamination of the spectra was removed utilising L2-regularisation (Bilgic et al., 2013). The resulting metabolite maps were interpolated spatially by a factor of two.

#### 2.6. Data evaluation

NAA SNR values were calculated via an adapted pseudo-replica method (Robson et al., 2008). Noise was assessed via the standard deviation of a Gaussian noise matrix generated for each coil channel, which was processed like the MRSI data. The signal amplitude was defined as the NAA peak heights of the LCModel estimation. The SNR values of all protocols with a TR 200 of ms were then corrected relative to protocol #2-“1SL\_M64\_TR600” by a factor of  $\frac{1}{\sqrt{5}}$  to account for an overestimation in the SNR calculation due to the different bandwidth and number of sampling points. The mean and standard deviation of NAA SNR, full width at half maximum (FWHM) and Cramér-Rao lower bounds (CRLBs) over all brain voxels of a scan protocol were compared between the protocols.

### 3. Results

#### 3.1. Simulation and parameter optimisation

The optimal average FA for a TR of 200 over all metabolites was 29°. The average magnetisation over all simulated metabolites was reduced to 58 ± 1% compared to a TR of 600 ms and to 38 ± 1% compared to a TR of 1500 ms. The highest change in ratios was between NAA and 3.9 ppm Cr, with a decrease of 2.5% from 600 to 200 ms and 4.3% from 1500 to 200 ms. Therefore, the expected change in the ratios between metabolites had only a negligible impact. While the SNR per excitation for NAA decreased to 58% of its value at a TR of 600 ms, the sensitivity  $\left(\frac{SNR}{\sqrt{F_{total}}}\right)$  remained the same (i.e., 100% of that obtained via protocol #1-“1SL\_M64\_TR600”).

**Table 2**

Mean NAA SNR, FWHM, and CRLB over all SSL and HSI volunteers. While the lower TR does not affect the SNR, FWHM and CRLB worsen due to the reduced spectral sampling. The sensitivity (here normalised to the square root of one hour) increases for the shorter TR, as it could be expected for more excitations in the same time. For different CAIPIRINHA accelerations of the UHR, sensitivity decreased by only a small amount due to noise enhancement.

	Protocol	NAA SNR	Sensitivity [ $1/\sqrt{h}$ ]	FWHM [Hz]	CRLB [%]
1SL	1SL_M64_TR600 R4	39 ± 13	110 ± 37	13 ± 4	4 ± 4
	1SL_M64_TR200 R4	22 ± 7	107 ± 35	18 ± 4	10 ± 5
	1SL_M128_TR200 R1	23 ± 8	27 ± 10	17 ± 5	10 ± 5
	1SL_M128_TR200 R2	16 ± 6	27 ± 10	19 ± 5	11 ± 5
	1SL_M128_TR200 R3	12 ± 5	26 ± 10	20 ± 5	13 ± 5
	1SL_M128_TR200 R4	10 ± 4	25 ± 9	21 ± 5	14 ± 6
	1SL_M128_TR200 R5	9 ± 4	25 ± 10	21 ± 5	15 ± 6
	1SL_M128_TR200 R6	8 ± 3	25 ± 10	22 ± 5	16 ± 7
	1SL_M128_TR200 R8	7 ± 3	25 ± 10	23 ± 6	17 ± 6
HSI	4SL_M64_TR200 R6	29 ± 11	247 ± 94	20 ± 6	9 ± 5
	4SL_M100_TR200 R6	19 ± 7	66 ± 26	13 ± 4	12 ± 6

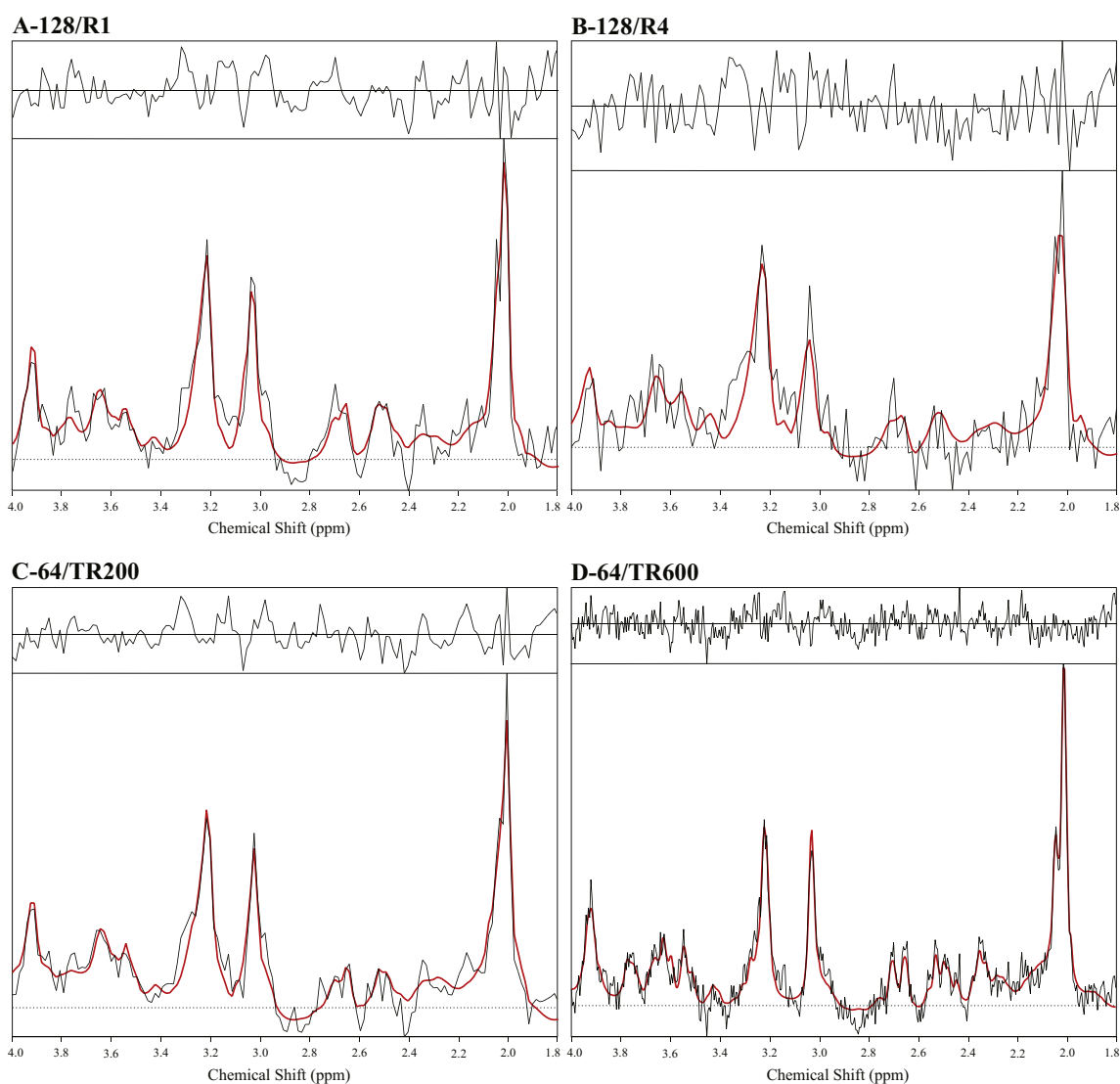


**Fig. 2.** Comparison of voxel spectra of the same occipital lobe WM location (note that UHR voxels are smaller by a factor of four) in the 1.8–4.0 ppm range, all with an acquisition delay of 1.3 ms. For the TR 200 ms protocols, a readout with 1024 sampling points/9000 Hz bandwidth was used and for the TR 600 ms protocol 2048 points/6000 Hz. Black is the measured spectrum and red the LCMoel-fitted metabolite resonances. The spectra were first-order phased for better visibility. A) Shows the non-accelerated UHR scan, b) the same scan artificially accelerated by a factor (R) of 4, C) the comparison measurement with the same TR of 200 ms and D) the comparison measurement with a TR of 600 ms. (For interpretation of the references to color in this figure legend, the reader is referred to the web version of this article).

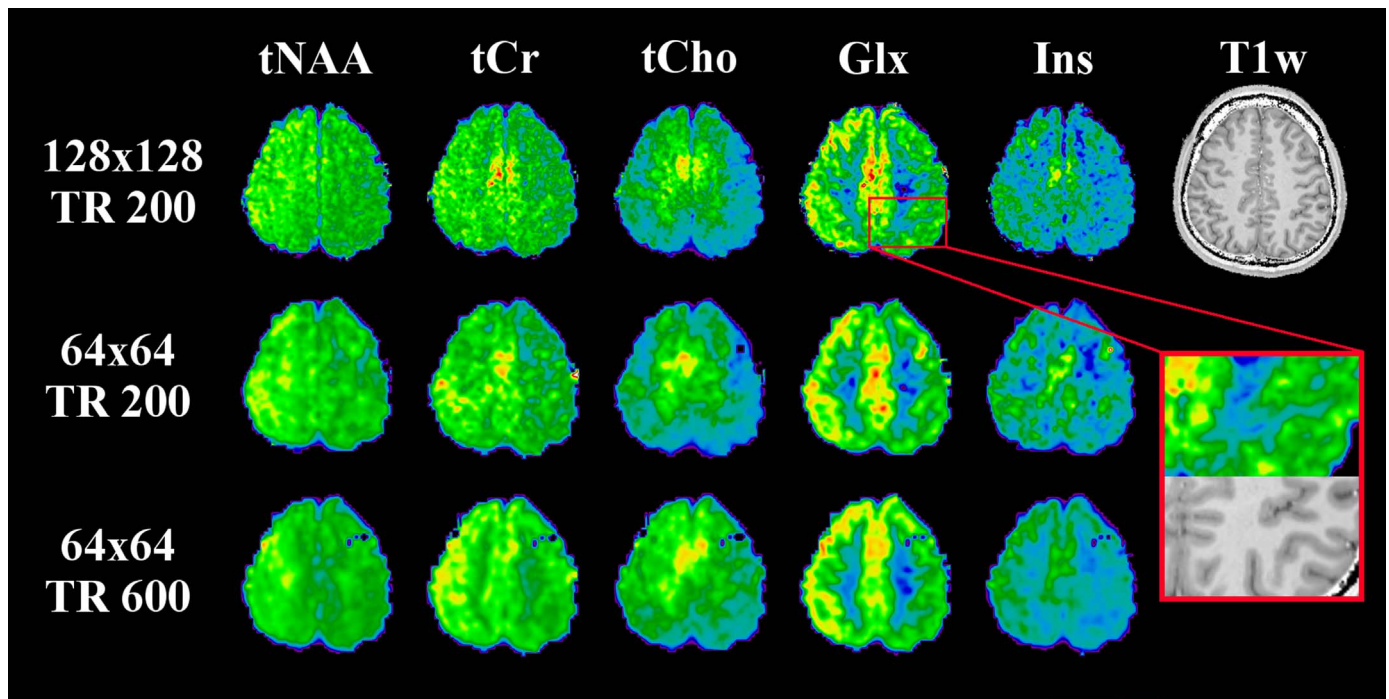


**Fig. 3.** UHR metabolite maps of one volunteer (without acceleration, measured, in decreasing order in 42, 2.5, and 7.5 min) show much greater correspondence to anatomical detail than the comparison maps, as in the cortical sulci or gyri, with  $tNAA=NAA+N$ -acetyl-aspartyl glutamate (NAAG),  $tCr=Cr$ +phosphocreatine (PCr),  $tCho$ =choline-containing compounds,  $Glx=Glu+glutamine$  (Gln). A zoom-in of the Glx-map highlights the visibility of the GM/WM contrast. The colours from cold to warm indicate higher relative concentrations, apart from the apparent concentration differences between the hemispheres that are most likely the result of the coil sensitivity profile if the subject's head is not exactly in the centre of the coil.

### 3.2. Volunteer measurements – Water suppression

The evaluation of WS efficiency showed a similar average remaining water signal of  $0.99 \pm 0.58\%$  to  $1.47 \pm 0.95\%$  for  $\tau$ s of 15–60 ms of the shortened four-pulse scheme (Supplementary Fig 1a). The longer three-pulse scheme resulted in an average of  $0.99 \pm 0.46\%$ . For  $\tau < 15$  ms, water sideband artefacts compromised the spectral quality (Supplementary Fig 1b). Therefore, with a  $\tau$  of 15 ms, WS duration could be minimised, with no loss of WS performance ( $1.14 \pm 0.65\%$  remaining water signal).

### 3.3. Volunteer measurements – Single-slice UHR

The average SNR values (Table 2) of protocol #1-“1SL\_M128\_TR200” and protocol #3-“1SL\_M64\_TR200”, were very similar ( $23 \pm 8$  and  $22 \pm 7$  respectively), as expected when accounting for the voxel volume, the encoding steps ( $\frac{1}{4} \times \sqrt{4} \times \sqrt{4}$ ) and acceleration compared to protocol #3-“1SL\_M64\_TR200”. The relative sensitivity was affected only by the different voxel volumes. Comparing protocols #1-“1SL\_M128\_TR200” and #2-“1SL\_M64\_TR600”, with the same factors for volume, encoding, and acceleration, there was a reduction of the SNR to 59%, very close to our simulation result of 58%. The relative sensitivity was slightly lower than the simulation (i.e., 97%). The reduction of sampling points from 2048 to 1024 over  $-5$  ppm to 10 pm affected the measured FWHM and CRLB values while the voxel volume did not. Sample spectra (Fig. 2) show that despite the reduced spectral sampling, the spectral information of UHR spectra remained similar. Metabolic maps obtained with protocol #1-“1SL\_M128\_TR200” reached a level of anatomical detail that showed gyri as well as the cortical sulci with an excellent GM/WM differentiation (Fig. 3), which was not possible with the  $64 \times 64$  matrix. The Glx-maps and also the ratio maps showed an excellent grey matter/white matter (GM/WM) contrast as displayed in Fig. 4 for all volunteers. Bland-Altman plots that compare the metabolite ratio of the protocols #2-“1SL\_M64\_TR600” and #3-“1SL\_M64\_TR200” (supplementary figure 3) show that the ratios of tNAA and Glx to tCr remain stable when

reducing the TR, but deviate for Ins and Cho.

The potential for measurement acceleration depends on the choice of metabolites that have to be reliably quantified (Fig. 5). While NAA offered enough signal to be accelerated by a factor of 6 (Tbl. 2), J-coupled metabolites, which are more challenging to detect, such as Ins or Glu, allowed acceleration by only 2–3-fold (i.e.,  $\sim 13$ –20 min scan time).

### 3.4. Phantom scans – HSI SNR and localisation

Slice profile measurements showed comparable slice profiles for single-slice and HSI measurements, with approximately 1–2% residual contamination per other slice for HSI (Supplementary Fig 2). Imperfect slice profiles for adjacent HSI slices required a small slice gap (25–50%) for *in vivo* measurements to avoid crosstalk between adjacent slices. Phantom experiments showed an Ac contamination of  $6.4 \pm 0.7\%$  for the single-slice,  $6.8 \pm 0.6\%$  for adjacent HSI, and  $6.5 \pm 1.1\%$  for HSI with a slice gap. This indicated that the contamination for HSI was similar to that of a single slice measurement. The SNR of the four-slice HSI scan was  $1.90 \pm 0.30$  higher than for the single-slice scan (i.e., close to the optimal factor of two).

### 3.5. Volunteer measurements – HSI-UHR

The average SNR for #5-“4SL\_M100\_TR200” of  $19 \pm 9$  (Tbl. 2) compared to protocol #1-“1SL\_M128\_TR200” was 17% lower rather than 5% higher, as we had estimated under 2.4.4. Therefore, the effective SNR-increase for HSI between protocol #1-“1SL\_M128\_TR200” and #5-“4SL\_M100\_TR200” was less than expected with a factor of 1.6 (an optimal factor of 2 was expected for four slices). The mean NAA CRLBs were  $12 \pm 5\%$ . The comparison of UHR- and the  $64 \times 64$  resolution reference measurement in one volunteer (Fig. 6) showed the increased metabolic map quality that can be already obtained with a  $100 \times 100$  matrix. This map quality was reproducible over all volunteers (Fig. 7). The metabolite and metabolic ratio maps of another volunteer (Fig. 8) showed that HSI-UHR-MRSI provides

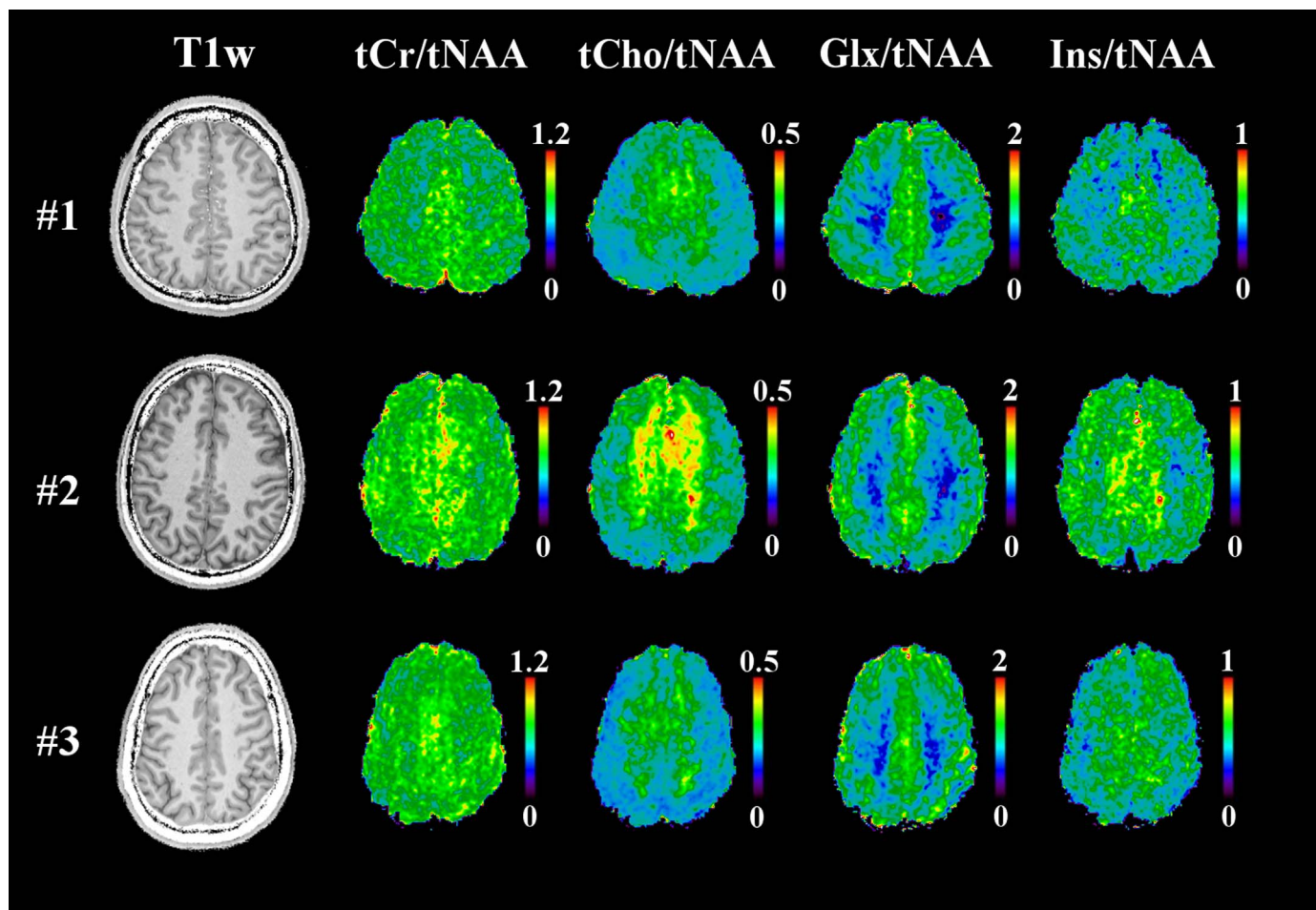


**Fig. 4.** UHR metabolic ratio maps of all three SSL volunteers acquired with protocol #1 1SL\_M128\_TR200 in 42 min. They consistently show a high grade of detail, and in the case of Glx/tNAA and tCho/tNAA, even a good GM/WM contrast.

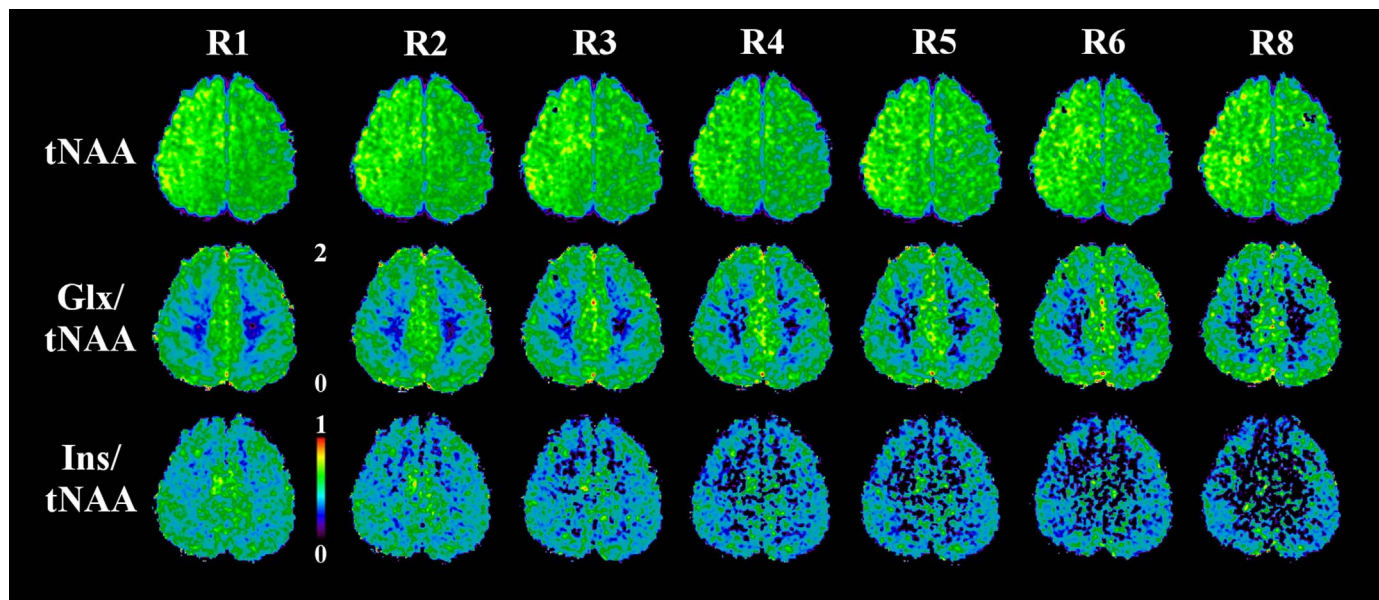


**Fig. 5.** The quality deterioration of the UHR-maps of protocol #1 1SL\_M128\_TR200 for increasing artificial acceleration factors (R) from 2 to 8 shows that, while the SNR for NAA is robust enough to allow higher accelerations, lower-SNR metabolites, e.g., Ins, can be reliably measured only with acceleration factors (R) of up to 2–4, depending on the required metabolites. This would still reduce the measurement time to 10–20 min, which is sufficient for clinical applications.

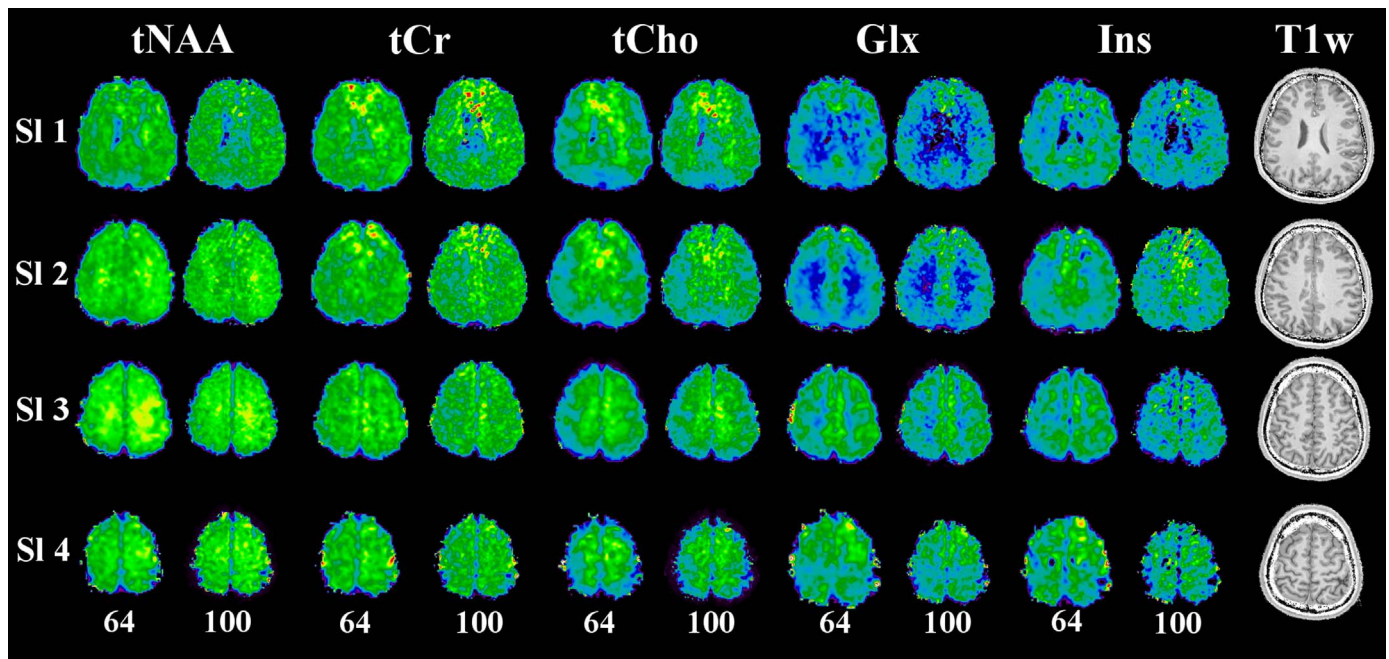


**Fig. 6.** A comparison of the metabolic maps for tNAA, tCr, tCho, Glx and Ins resulting from measurements with 64×64- and 100×100 matrix size (protocols 4SL\_M64\_TR200 and 4SL\_M100\_TR200, see Tbl. 1) for one volunteer shows that both allow the creation of high-quality 3D-MRSI maps. The higher resolution allows a clearer separation of anatomical regions and shows more correspondence to the gyri, especially in the upper slices, but also display more artefacts, as seen in the frontal regions of the slices 1 and 2. The colours from cold to warm indicate higher relative concentrations.

visibility of similar anatomical structures and GM/WM contrast similar to that of 1SL-UHR-MRSI, but provided superior brain coverage.

#### 4. Discussion

The presented phantom and volunteer results show that single- and multi-slice UHR-FID-MRSI in the brain are feasible at 7 T, and provide high-resolution metabolic maps in clinically acceptable measurement times.

##### 4.1. Results in comparison to other research

###### 4.1.1. Acquisition and TR reduction

Improving WET WS timing with shorter gradients allowed shorter TRs while retaining similar WS quality. Our simulations showed that the shorter TRs did not lead to a relevant change in metabolite ratios due to changed  $T_1$ -weighting (but could be corrected for if desired). In contrast to FID-MRSI (Boer et al., 2011; Bogner et al., 2012) for  $\geq 7$  T, which allows extremely short TRs due to its simple pulse scheme, alternatives acquisition approaches like semi-LASER (Scheenen et al., 2008) or PRESS (Balchandani et al., 2008; Xu et al., 2008) are limited to an ROI in the centre of the brain and lower matrix sizes. In contrast, the FID-based approach without outer volume suppression enables coverage of the whole slice, including locations including the subcortical and cortical regions of the brain.

###### 4.1.2. Acceleration methods

Our results show that acceleration of single-slice MRSI by a factor of 2–3 is possible with parallel imaging, while retaining enough SNR for reliable quantification of metabolites. Even higher acceleration factors of up to 6 were reliable for HSI measurements due to the increased SNR. We previously showed that the use of prescan imaging data as an auto-calibration signal to accelerate MRSI measurements with GRAPPA (Hangel et al., 2015) or CAIPIRINHA (Strasser et al., 2016, Nr. 0651) allowed acceleration factors up to 9 with g-factors < 1.1 than reported for SENSE approaches at 7 T thus far (Kirchner et al., 2015; Zhu et al., 2013).

Parallel imaging efficiency benefits substantially from higher  $B_0$  and improved receive coils (Wiesinger et al., 2004). In contrast, EPSI and spiral sampling benefit mostly from improved gradient hardware, but are challenging at higher  $B_0$  (e.g., 7 T), even with lower resolution. While EPSI that measured a 32×32 matrix in 8:32 min with a spectral BW of 1380 Hz was presented in 2006 (Otazo et al., 2006), this required a special head gradient (e.g. 80 mT/m, 600 mT/m/ms). Although recently (Snoussi et al., ISMRM 2015, Nr. 0428) presented EPSI with a 50×50×18 matrix at 7 T in 25 min and a spectral readout BW of 2466 Hz, the gradient restrictions of whole-body scanners limit the SNR efficiency compared to 3 T. The combination of both PI and spectral-spatial sampling could combine the benefits of both (Sabati et al., 2014).

###### 4.1.3. Ultra-high resolution

To our knowledge, we present the first MRSI sequence for human brain scanning at 7 T *in vivo* that allows matrix sizes of up to 128×128 and nominal spatial resolutions as low as 23 mm<sup>3</sup> within clinically feasible scan times. At 3 T, where acquisition strategies with advanced readout trajectories are commonly used due to the lower required receiver bandwidth, UHR-MRSI has been reported. With a combination of phase encoded MRSI and EPSI sampling, a 110×110 matrix was acquired in 15.5 min (Ma et al., 2016), as well as an 80×80×20 matrix in 26 min (Lam et al., 2015). Furthermore, by using spiral MRSI with a reduced spectral BW of ~600 Hz (Bhattacharya and Jacob, ISMRM 2015, Nr. 2017), matrix sizes of 96×96 in 3 min and 128×128 in 7 min were achieved.

###### 4.1.4. Hadamard spectroscopy imaging

While it was necessary to reduce the matrix size to 100×100 for four-slice HSI to keep measurement times short, the cascaded approach offered accurate localisation and low SAR. The SNR was increased 1.6-fold compared to single-slice acquisition, but theoretical predictions were not entirely fulfilled. This could be explained by the larger brain coverage that makes our acquisitions more prone to  $B_0/B_1^+$ -inhomogeneities as well as partial volume effects from ventricles, compared to single-slice MRSI. Traditional HSI using superimposed

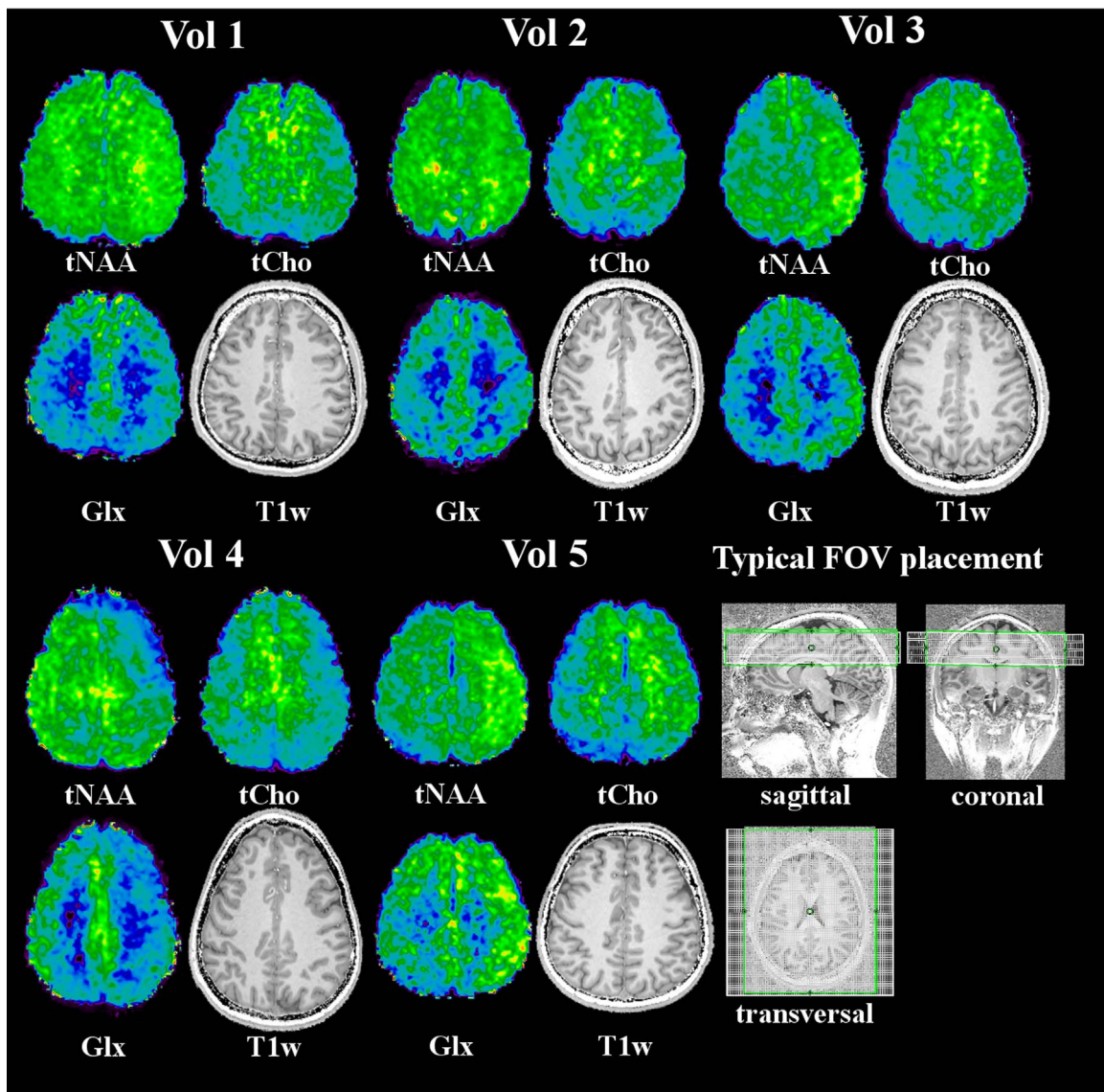


**Fig. 7.** Metabolic maps (tNAA, tCho, Glx) of slice 2 for all five volunteers measured with the 4SL\_M100\_TR200 protocol in 17 min as well as an example of the typical placement of the MRSI matrix. The quality is similar over all measurements (like the GM/WM contrast for the tCho and Glx maps), but three of the volunteers' maps show signal inhomogeneity from one side to the other that can be removed by the calculation of metabolic ratios (see Fig. 8). The colours from cold to warm indicate higher relative concentrations.

pulses is impractical at  $\geq 7$  T, and thus, HSI has so far not found wide application, although cascaded HSI was shown to overcome major technical problems at 7 T (Goelman et al., 2007). In comparison, HSI was recently employed at 3 T, e.g., for multi-slice rosette-trajectory MRSI (Schirda et al., ISMRM 2015, Nr. 0987).

#### 4.1.5. Lipid artefact removal

Lipid removal during data processing using L2-regularisation (Bilgic et al., 2013), as in our study, can reduce lipid signals by a lipid suppression factor (LSF) of 9–10. This method is computationally demanding, but does not negatively affect SAR, measurement time, or localisation and does not require additional measurement equipment. In comparison, other lipid suppression methods at 7 T were able to reach higher LSFs, but had some drawbacks. FIDLOVS (Henning et al., 2009) outer volume suppression achieved an LSF of 25, but prolonged the minimum TR to 5 s to stay within SAR constraints. SWAMP water/lipid suppression (Boer et al., 2011), limited to an ROI, featured an LSF of 4–5. Non-selective DIR-based lipid suppression (Hangel et al., 2015) reached an LSF of 13, but sacrificed  $\sim 50\%$  of the SNR and increased the minimum TR. Spatial-spectral outer volume suppression (Balchandani and Spielman, 2008) resulted in an LSF of 7, but also a

loss of metabolite signal between 3.2 and 4.7 ppm in the brain periphery. Slice-selective hyperbolic secant pulses combined with dynamic  $B_0$ -shimming (Boer et al., 2012), allowed an LSF of  $\sim 30$  but the setup was time-consuming (i.e.,  $\sim 10$  min). Using additional hardware, such as an eight-channel transmission array for ring-shaped  $B_1^+$ -excitation of subcutaneous lipids (Hetherington et al., 2010), allowed an LSF of 58, while an additional crusher coil activated during the TE (Boer et al., 2015) achieved LSFs of 20–70.

#### 4.1.6. Ultra-high resolution metabolite mapping

The resulting metabolite maps of the brain show unmatched detail that allows the study of small focal regions. On the NAA maps the hemispheres, ventricles, gyri and cerebrospinal fluid (CSF) are clearly distinguishable. Cho- and Glx-maps show the expected strong GM/WM contrast. The clearly visible Cho hotspot in the mesial frontal grey matter is likely linked to the cingulate gyrus (Degaonkar et al., 2005).

#### 4.2. Advantages and limitations

The main advantages of the proposed UHR-FID-MRSI approach are the high in-plane resolution and full slice coverage without ROI

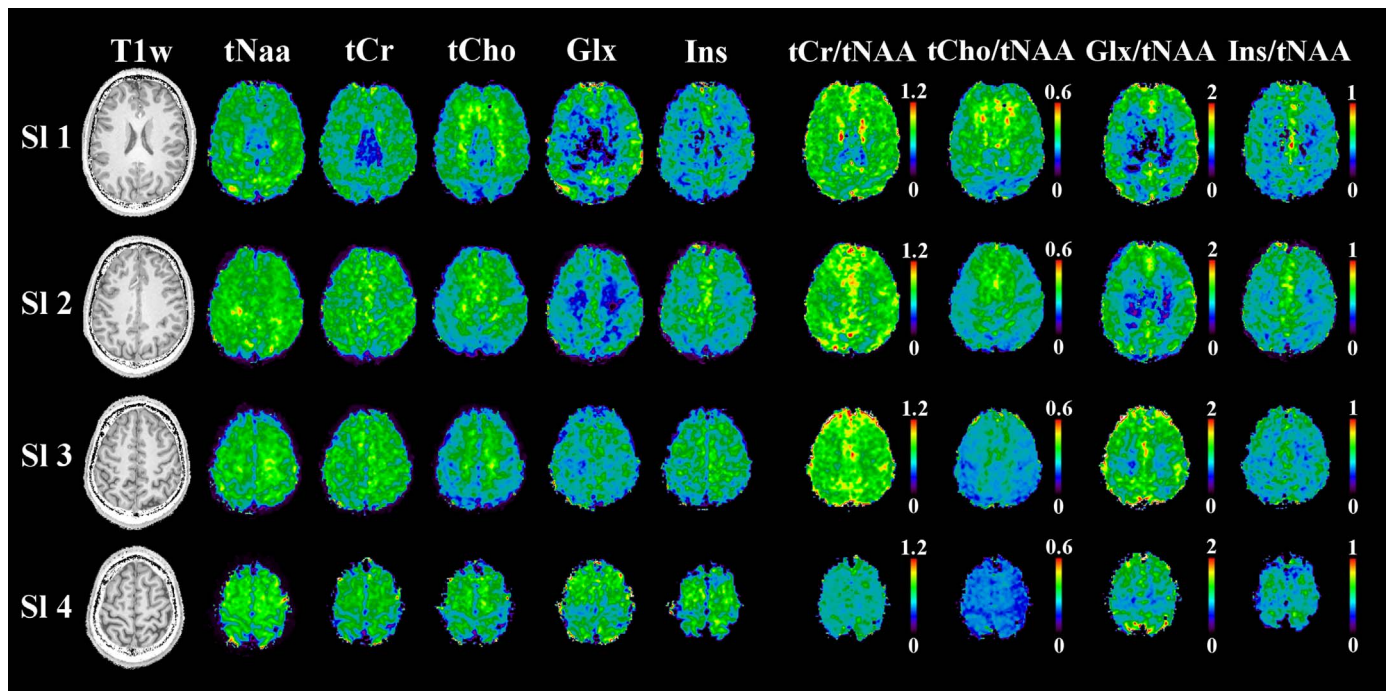


**Fig. 8.** Detailed view of all four slices for one of the volunteers measured with the 4SL\_M100\_TR200 protocol in 17 min, including metabolite (tNAA, tCr, tCho, Glx, and Ins) and metabolic ratio maps (tCr/tNAA, tCho/tNAA, Glx/tNAA, Ins/tNAA). Structures like ventricles and gyri are visible on the metabolic maps. On the ratio maps, the expected change in ratios due to the increase of grey matter in the slice can be clearly seen. The colours from cold to warm indicate higher relative concentrations.

restrictions, but within clinically feasible scan times. The resulting small voxel size reduces partial volume effects substantially. HSI extends this method to a limited number of slices while increasing the available SNR without the drawbacks associated with phase encoding in the z-direction. A major disadvantage of the cascaded approach is the slightly different TEs or ADs for different slices, which may be overcome by the design of recently proposed multi-band RF pulses (Feinberg and Setsompop, 2013; Koopmans et al., 2013).

CAIPRINHA acceleration with imaging prescans as auto-calibration data is very efficient at 7 T with a 32-channel array coil (Hangel et al., 2015). The exact resolution and measurement time for a desired protocol are a trade-off between SNR/spectral quality, measurement time, and resolution. This makes UHR-MRSI a flexible clinical research tool for matrix sizes from  $64 \times 64$  to  $128 \times 128$  and one to four slices.

Slice placement is limited by field inhomogeneities, particularly in  $B_0$ , while it is less sensitive to  $B_1^+$  errors than other MRSI approaches. If no additional  $B_0$  shimming (Hetherington et al., 2014; Pan et al., 2012; Stockmann et al., 2015) is used, our approach is, thus, currently limited to regions at the level of the ventricles and above. Due to the desired short measurement times, HSI for multi-slice MRSI is limited to a maximum of four slices, which is sufficient to cover the brain from the ventricles upward, with an  $\sim 4$  cm thick slab. In combination with spatial-spectral sampling methods, PI could achieve far higher acceleration, which would offer superior brain coverage (Sabati et al., 2014; Tsai et al., 2008).

A reduced readout duration can lead to truncation artefacts of the FID, which could occur when  $T_2^*$ s increase due to a better  $B_0$ -shim. This could bias the quantification of low abundant (J-coupled) metabolites.

Motion reduces spectral quality and leads to substantial lipid artefacts. Movement artefacts can be reduced by keeping scan times short, which is essential for noncompliant subjects. Real-time motion correction can further improve data quality (Bogner et al., 2014, 2013). In our study we removed lipid artefacts by L2-regularisation, which avoids the drawbacks of other lipid suppression schemes (see 4.1.5.).

#### 4.3. Outlook

The introduction of additional hardware- or software-based methods will further improve data quality. Possible technical improvements include higher-order  $B_0$ -shims (Hetherington et al., 2014; Pan et al., 2012), dynamic shims (Boer et al., 2012; Duerst et al., 2015), or enhanced  $B_0$ -shimming algorithms (Fillmer et al., 2015), as well as  $B_1^+$ -shimming with parallel transmit systems (Boer et al., 2012; Emir et al., 2012). Real-time motion correction (Bogner et al., 2013) will further increase the reliability of our MRSI acquisition strategy. Better gradient coils and reconstruction software will enhance the performance of accelerated high-resolution MRSI. Most of these improvements will improve SNR, which can be translated into higher acceleration, and thus, reduced measurement times or increased (multi-slice) brain coverage.

In any case, UHR-MRSI could be applied to clinical research questions, such as previously demonstrated for glioma (Li et al., 2015)(Chadzynski et al., ISMRM 2015, Nr. 0763), Multiple Sclerosis (Srinivasan et al., 2010), brain injury (Hetherington et al., 2014), Adrenoleukodystrophy (Ratai et al., 2008), and the study of Alzheimer's disease, Parkinson's disease, and Epilepsy (Pan et al., 2013). Apart from these clinical applications, UHR-MRSI in volunteers would allow a highly detailed biochemical reference “atlas” to be established to aid future brain research and study of the normal aging brain (Lecocq et al., 2015).

## 5. Conclusions

We successfully demonstrated that the benefits of 7 T systems, i.e., improved SNR and increased spectral dispersion, can be translated into clinically feasible multi-slice FID-MRSI with ultra-high spatial resolution mapping ( $< 2 \times 2$  mm<sup>2</sup> with a  $128 \times 128$  matrix) of several important chemical compounds. This will facilitate the application of MRSI to clinical and neuro-scientific research problems where the visualization of small details is mandatory (e.g., small Multiple Sclerosis lesions). In summary, UHR-MRSI within clinically applicable measure-

ment times, as presented here, is a powerful imaging tool that shows the benefits that  $\geq 7$  T systems offer.

## Acknowledgements

This study was supported by the Austrian Science Fund (FWF): KLI-61, the FFG Bridge Early Stage Grant #846505 and the Christian Doppler Laboratory for Clinical Molecular MR Imaging.

## Appendix A. Supplementary material

Supplementary data associated with this article can be found in the online version at <http://dx.doi.org/10.1016/j.neuroimage.2016.10.043>.

## References

- Andronesi, O.C., Gagoski, B.A., Sorensen, A.G., 2012. Neurologic 3D MR spectroscopic imaging with low-power adiabatic pulses and fast spiral acquisition. *Radiology* 262, 647–661. <http://dx.doi.org/10.1148/radiol.11110277>.
- Avdievich, N.I., Pan, J.W., Baehring, J.M., Spencer, D.D., Hetherington, H.P., 2009. Short echo spectroscopic imaging of the human brain at 7T using transceiver arrays. *Magn. Reson. Med.* 62, 17–25. <http://dx.doi.org/10.1002/mrm.21970>.
- Balchandani, P., Pauly, J., Spielman, D., 2008. Interleaved narrow-band PRESS sequence with adiabatic spatial-spectral refocusing pulses for  $^1\text{H}$  MRSI at 7T. *Magn. Reson. Med.* 59, 973–979. <http://dx.doi.org/10.1002/mrm.21539>.
- Balchandani, P., Spielman, D., 2008. Fat suppression for  $^1\text{H}$  MRSI at 7T using spectrally selective adiabatic inversion recovery. *Magn. Reson. Med.* 59, 980–988. <http://dx.doi.org/10.1002/mrm.21537>.
- Bilgic, B., Chatnuntawech, I., Fan, A.P., Setsompop, K., Cauley, S.F., Wald, L.L., Adalsteinsson, E., 2013. Fast image reconstruction with L2-regularization. *J. Magn. Reson. Imaging* 00, 1–11. <http://dx.doi.org/10.1002/jmri.24365>.
- Boer, V.O., Siero, J.C.W., Hoogduin, H., van Gorp, J.S., Luijten, P.R., Klomp, D.W.J., 2011. High-field MRS of the human brain at short TE and TR. *NMR Biomed.* 24, 1081–1088. <http://dx.doi.org/10.1002/nbm.1660>.
- Boer, V.O., Klomp, D.W.J., Juchem, C., Luijten, P.R., de Graaf, R.A., 2012. Multislice  $^1\text{H}$  MRSI of the human brain at 7 T using dynamic B0 and B1 shimming. *Magn. Reson. Med.* 68, 662–670. <http://dx.doi.org/10.1002/mrm.23288>.
- Boer, V.O., van de Lindt, T., Luijten, P.R., Klomp, D.W.J., 2015. Lipid suppression for brain MRI and MRSI by means of a dedicated crusher coil. *Magn. Reson. Med.* 73, 2062–2068. <http://dx.doi.org/10.1002/mrm.25331>.
- Bogner, W., Gruber, S., Trattinig, S., Chmelik, M., 2012. High-resolution mapping of human brain metabolites by free induction decay  $^1\text{H}$  MRSI at 7T. *NMR Biomed.* 25, 873–882. <http://dx.doi.org/10.1002/nbm.1805>.
- Bogner, W., Hess, A.T., Gagoski, B., Tisdall, M.D., van der Kouwe, A.J.W., Trattinig, S., Rosen, B., Andronesi, O.C., 2013. Real-time motion- and B0-correction for LASER-localized spiral-accelerated 3D-MRSI of the brain at 3T. *Neuroimage* 88C, 22–31. <http://dx.doi.org/10.1016/j.neuroimage.2013.09.034>.
- Bogner, W., Gagoski, B., Hess, A.T., Bhat, H., Tisdall, M.D., van der Kouwe, A.J.W., Strasser, B., Marjańska, M., Trattinig, S., Grant, E., Rosen, B., Andronesi, O.C., 2014. 3D GABA imaging with real-time motion correction, shim update and reacquisition of adiabatic spiral MRSI. *Neuroimage* 103, 290–302. <http://dx.doi.org/10.1016/j.neuroimage.2014.09.032>.
- Bottomey, P.A., Ouwerkerk, R., 1994. Optimum flip-angles for exciting NMR with uncertain T1 values. *Magn. Reson. Med.* 32, 137–141.
- Chung, S., Kim, D., Breton, E., Axel, L., 2010. Rapid B1+ mapping using a preconditioning RF pulse with TurboFLASH readout. *Magn. Reson. Med.* 64, 439–446. <http://dx.doi.org/10.1002/mrm.22423>.
- Degaonkar, M.N., Pomper, M.G., Barker, P.B., 2005. Quantitative proton magnetic resonance spectroscopic imaging: regional variations in the corpus callosum and cortical gray matter. *J. Magn. Reson. Imaging* 22, 175–179. <http://dx.doi.org/10.1002/jmri.20353>.
- Duerst, Y., Wilm, B.J., Dietrich, B.E., Vannesjo, S.J., Barmet, C., Schmid, T., Brunner, D.O., Pruessmann, K.P., 2015. Real-time feedback for spatiotemporal field stabilization in MR systems. *Magn. Reson. Med.* 73, 884–893. <http://dx.doi.org/10.1002/mrm.25167>.
- Emir, U.E., Auerbach, E.J., Moortele, Van De, P.-F., Marjańska, M., Uğurbil, K., Terpstra, M., Tkáč, I., Öz, G., 2012. Regional neurochemical profiles in the human brain measured by  $^1\text{H}$  MRS at 7 T using local B1 shimming. *NMR Biomed.* 25, 152–160. <http://dx.doi.org/10.1002/nbm.1727>.
- Feinberg, D.A., Setsompop, K., 2013. Ultra-fast MRI of the human brain with simultaneous multi-slice imaging. *J. Magn. Reson.* 229, 90–100. <http://dx.doi.org/10.1016/j.jmr.2013.02.002>.
- Fillmer, A., Kirchner, T., Cameron, D., Henning, A., 2015. Constrained image-based B0 shimming accounting for “local minimum traps” in the optimization and field inhomogeneities outside the region of interest. *Magn. Reson. Med.* 73, 1370–1380. <http://dx.doi.org/10.1002/mrm.25248>.
- Goelman, G., Liu, S., Fleysher, R., Fleysher, L., Grossman, R.I., Gonen, O., 2007. Chemical-shift artifact reduction in hadamard-encoded MR spectroscopic imaging at high (3T and 7T) magnetic fields. *Magn. Reson. Med.* 58, 167–173. <http://dx.doi.org/10.1002/mrm.21251>.
- Hangel, G., Strasser, B., Považan, M., Gruber, S., Chmelik, M., Gajdošik, M., Trattinig, S., Bogner, W., 2015. Lipid suppression via double inversion recovery with symmetric frequency sweep for robust 2D-GRAPPA-accelerated MRSI of the brain at 7 T. *NMR Biomed.* 28, 1413–1425. <http://dx.doi.org/10.1002/nbm.3386>.
- Henning, A., Fuchs, A., Murdoch, J.B., Boesiger, P., 2009. Slice-selective FID acquisition, localized by outer volume suppression (FIDLOVS) for  $^1\text{H}$ -MRSI of the human brain at 7 T with minimal signal loss. *NMR Biomed.* <http://dx.doi.org/10.1002/nbm.1366>.
- Hetherington, H.P., Avdievich, N.I., Kuznetsov, A.M., Pan, J.W., 2010. RF shimming for spectroscopic localization in the human brain at 7 T. *Magn. Reson. Med.* 63, 9–19. <http://dx.doi.org/10.1002/mrm.22182>.
- Hetherington, H.P., Hamid, H., Kulas, J., Ling, G., Bandak, F., de Lanerolle, N.C., Pan, J.W., 2014. MRSI of the medial temporal lobe at 7 T in explosive blast mild traumatic brain injury. *Magn. Reson. Med.* 71, 1358–1367. <http://dx.doi.org/10.1002/mrm.24814>.
- Kirchner, T., Fillmer, A., Tsao, J., Pruessmann, K.P., Henning, A., 2015. Reduction of voxel bleeding in highly accelerated parallel  $^1\text{H}$  MRSI by direct control of the spatial response function. *Magn. Reson. Med.* 73, 469–480. <http://dx.doi.org/10.1002/mrm.25185>.
- Klose, U., 1992. Mapping of the radio frequency magnetic field with a MR snapshot FLASH technique. *Med. Phys.* 19, 1099–1104.
- Koopmans, P.J., Boyacıoğlu, R., Barth, M., Norris, D.G., 2013. Simultaneous multislice inversion contrast imaging using power independent of the number of slices (PINS) and delays alternating with nutation for tailored excitation (DANTE) radio frequency pulses. *Magn. Reson. Med.* 69, 1670–1676. <http://dx.doi.org/10.1002/mrm.24402>.
- Lam, F., Ma, C., Clifford, B., Johnson, C.L., Liang, Z.-P., 2015. High-resolution  $^1\text{H}$ -MRSI of the brain using SPICE: data acquisition and image reconstruction. *Magn. Reson. Med.* <http://dx.doi.org/10.1002/mrm.26019>, (N/a–N/a).
- Lecocq, A., Le Fur, Y., Maudsley, A. a, Le Troter, A., Sheriff, S., Sabati, M., Donnadieu, M., Confort-Gouny, S., Cozzone, P.J., Guye, M., Ranjeva, J.-P., 2014. Whole-brain quantitative mapping of metabolites using short echo three-dimensional proton MRSI. *J. Magn. Reson. Imaging*, 1–10. <http://dx.doi.org/10.1002/jmri.24809>.
- Lecocq, A., Le Fur, Y., Maudsley, A. a, Le Troter, A., Sheriff, S., Sabati, M., Donnadieu, M., Confort-Gouny, S., Cozzone, P.J., Guye, M., Ranjeva, J.-P., 2015. Whole-brain quantitative mapping of metabolites using short echo three-dimensional proton MRSI. *J. Magn. Reson. Imaging* 42, 280–289. <http://dx.doi.org/10.1002/jmri.24809>.
- Li, Y., Larson, P., Chen, A.P., Lupo, J.M., Ozhinsky, E., Kelley, D., Chang, S.M., Nelson, S.J., 2015. Short-echo three-dimensional H-1 MR spectroscopic imaging of patients with glioma at 7 T for characterization of differences in metabolite levels. *J. Magn. Reson. Imaging* 41, 1332–1341. <http://dx.doi.org/10.1002/jmri.24672>.
- Ma, C., Lam, F., Ning, Q., Johnson, C.L., Liang, Z.-P., 2016. High-resolution  $^1\text{H}$ -MRSI of the brain using short-TE SPICE. *Magn. Reson. Med.* <http://dx.doi.org/10.1002/mrm.26130>, (N/a–N/a).
- Marques, J.P., Kober, T., Krueger, G., van der Zwaag, W., Van de Moortele, P.-F., Gruetter, R., 2010. MP2RAGE, a self bias-field corrected sequence for improved segmentation and T1-mapping at high field. *Neuroimage* 49, 1271–1281. <http://dx.doi.org/10.1016/j.neuroimage.2009.10.002>.
- Moser, E., Stahlberg, F., Ladd, M.E., Trattinig, S., 2012. 7-T MR—from research to clinical applications? *NMR Biomed.* 25, 695–716. <http://dx.doi.org/10.1002/nbm.1794>.
- Ogg, R.J., Kingsley, P.B., Taylor, J.S., 1994. WET, a T1- and B1-insensitive water-suppression method for in vivo localized  $^1\text{H}$  NMR spectroscopy. *J. Magn. Reson. B* 104, 1–10.
- Otazo, R., Mueller, B., Ugurbil, K., Wald, L., Posse, S., 2006. Signal-to-noise ratio and spectral linewidth improvements between 1.5 and 7 T in proton echo-planar spectroscopic imaging. *Magn. Reson. Med.* 56, 1200–1210. <http://dx.doi.org/10.1002/mrm.21067>.
- Pan, J.W., Lo, K.-M., Hetherington, H.P., 2012. Role of very high order and degree B0 shimming for spectroscopic imaging of the human brain at 7 T. *Magn. Reson. Med.* 68, 1007–1017. <http://dx.doi.org/10.1002/mrm.24122>.
- Pan, J.W., Duckrow, R.B., Gerrard, J., Ong, C., Hirsch, L.J., Resor, S.R., Zhang, Y., Petroff, O., Spencer, S., Hetherington, H.P., Spencer, D.D., 2013. 7T MR spectroscopic imaging in the localization of surgical epilepsy. *Epilepsia* 54, 1668–1678. <http://dx.doi.org/10.1111/epi.12322>.
- Pohmann, R., von Kienlin, M., Haase, A., 1997. Theoretical evaluation and comparison of fast chemical shift imaging methods. *J. Magn. Reson.* 129, 145–160. <http://dx.doi.org/10.1006/jmre.1997.1245>.
- Považan, M., Hangel, G., Strasser, B., Gruber, S., Chmelik, M., Trattinig, S., Bogner, W., 2015. Mapping of brain macromolecules and their use for spectral processing of (1) H-MRSI data with an ultra-short acquisition delay at 7T. *Neuroimage* 121, 126–135. <http://dx.doi.org/10.1016/j.neuroimage.2015.07.042>.
- Provencher, S.W., 2001. Automatic quantitation of localized in vivo  $^1\text{H}$  spectra with LCMODEL. *NMR Biomed.* 14, 260–264. <http://dx.doi.org/10.1002/nbm.698>.
- Ratai, E., Kok, T., Wiggins, C., Wiggins, G., Grant, E., Gagoski, B., O'Neill, G., Adalsteinsson, E., Eichler, F., 2008. Seven-Tesla proton magnetic resonance spectroscopic imaging in adult X-linked adrenoleukodystrophy. *Arch. Neurol.* 65, 1488–1494. <http://dx.doi.org/10.1001/archneur.65.11.1488>.
- Robson, P.M., Grant, A.K., Madhuranthakam, A.J., Lattanzi, R., Sodickson, D.K., McKenzie, C. a, 2008. Comprehensive quantification of signal-to-noise ratio and g-factor for image-based and k-space-based parallel imaging reconstructions. *Magn. Reson. Med.* 60, 895–907. <http://dx.doi.org/10.1002/mrm.21728>.
- Sabati, M., Zhan, J., Govind, V., Arheart, K.L., Maudsley, A. a, 2014. Impact of reduced k-space acquisition on pathologic detectability for volumetric MR spectroscopic imaging. *J. Magn. Reson. Imaging* 39, 224–234. <http://dx.doi.org/10.1002/jmri.24130>.

- Scheenen, T.W.J., Heerschap, A., Klomp, D.W.J., 2008. Towards  $^1\text{H}$ -MRSI of the human brain at 7T with slice-selective adiabatic refocusing pulses. *MAGMA* 21, 95–101. <http://dx.doi.org/10.1007/s10334-007-0094-y>.
- Schirda et al., ISMRM 2015, Nr. 0987, Rosette Spectroscopic Imaging with Hadamard Encoding, Claudiu Schirda, Tiejun Zhao, Julie Pan, and Hoby Hetherington
- Snoussi et al., ISMRM 2015, Nr. 0428, Adapting volumetric 1H echo-planar spectroscopic imaging of the human brain from 3 to 7 Tesla, Karim Snoussi, Joseph S. Gillen, Michael Schär, Richard A.E. Edden, Andrew A. Maudsley, and Peter B. Barker
- Srinivasan, R., Ratiney, H., Hammond-Rosenbluth, K.E., Pelletier, D., Nelson, S.J., 2010. MR spectroscopic imaging of glutathione in the white and gray matter at 7 T with an application to multiple sclerosis. *Magn. Reson. Imaging* 28, 163–170. <http://dx.doi.org/10.1016/j.mri.2009.06.008>.
- Stockmann, J.P., Witzel, T., Keil, B., Polimeni, J.R., Mareyam, A., LaPierre, C., Setsompop, K., Wald, L.L., 2015. A 32-channel combined RF and B0 shim array for 3T brain imaging. *Magn. Reson. Med.* 00, 1–11. <http://dx.doi.org/10.1002/mrm.25587>.
- Strasser, B., Chmelik, M., Robinson, S.D., Hangel, G., Gruber, S., Trattng, S., Bogner, W., 2013. Coil combination of multichannel MRSI data at 7 T: musical. *NMR Biomed.* 26, 1796–1805. <http://dx.doi.org/10.1002/nbm.3019>.
- Strasser, B., Považan, M., Hangel, G., Hingerl, L., Chmelik, M., Gruber, S., Trattng, S., Bogner, W., 2016. (2+1)D-CAIPIRINHA Accelerated MR Spectroscopic Imaging of the Brain at 7 T. *Magn. Reson. Med.* [details will be added proofing].
- Tsai, S.-Y., Otazo, R., Posse, S., Lin, Y.-R., Chung, H.-W., Wald, L.L., Wiggins, G.C., Lin, F.-H., 2008. Accelerated proton echo planar spectroscopic imaging (PEPSI) using GRAPPA with a 32-channel phased-array coil. *Magn. Reson. Med.* 59, 989–998. <http://dx.doi.org/10.1002/mrm.21545>.
- Wiesinger, F., Van de Moortele, P.-F., Adriany, G., De Zanche, N., Ugurbil, K., Pruessmann, K.P., 2004. Parallel imaging performance as a function of field strength—an experimental investigation using electrodynamic scaling. *Magn. Reson. Med.* 52, 953–964. <http://dx.doi.org/10.1002/mrm.20281>.
- Xin, L., Schaller, B., Mlynarik, V., Lu, H., Gruetter, R., 2013. Proton T1 relaxation times of metabolites in human occipital white and gray matter at 7 T. *Magn. Reson. Med.* 69, 931–936. <http://dx.doi.org/10.1002/mrm.24352>.
- Xu, D., Cunningham, C.H., Chen, A.P., Li, Y., Kelley, D. a C., Mukherjee, P., Pauly, J.M., Nelson, S.J., Vigneron, D.B., 2008. Phased array 3D MR spectroscopic imaging of the brain at 7 T. *Magn. Reson. Imaging* 26, 1201–1206. <http://dx.doi.org/10.1016/j.mri.2008.03.006>.
- Zhu, H., Soher, B.J., Ouwerkerk, R., Schär, M., Barker, P.B., 2013. Spin-echo magnetic resonance spectroscopic imaging at 7 T with frequency-modulated refocusing pulses. *Magn. Reson. Med.* 69, 1217–1225. <http://dx.doi.org/10.1002/mrm.24357>.